ARL-TR-10307 • MAR 2026

Influence of Chirality on the Energy Release Behavior of a Molecular Ferroelectric Energetic Material

by Jennifer L. Gottfried, Lauren B. Blaudeau, and Shenqiang Ren

NOTICES

Disclaimers

The findings in this report are not to be construed as an official Department of the Army position unless so designated by other authorized documents.

Citation of manufacturer's or trade names does not constitute an official endorsement or approval of the use thereof.

Destroy this report when it is no longer needed. Do not return it to the originator.

ARL-TR-10307 ● MAR 2026

Influence of Chirality on the Energy Release Behavior of a Molecular Ferroelectric Energetic Material

Jennifer L. Gottfried and Lauren B. Blaudeau
DEVCOM Army Research Laboratory

Shenqiang Ren
University of Maryland

REPORT DOCUMENTATION PAGE

1. REPORT DATE	2. REPORT TYPE	3. DATES COVERED	
		START DATE	END DATE
March 2026	Technical Report	10 September 2025	12 February 2026

4. TITLE AND SUBTITLE
Influence of Chirality on the Energy Release Behavior of a Molecular Ferroelectric Energetic Material

5a. CONTRACT NUMBER	5b. GRANT NUMBER	5c. PROGRAM ELEMENT NUMBER
CRADA-20-048-J001		
5d. PROJECT NUMBER	**5e. TASK NUMBER**	**5f. WORK UNIT NUMBER**

6. AUTHOR(S)
Jennifer L. Gottfried, Lauren B. Blaudeau, and Shenqiang Ren

7. PERFORMING ORGANIZATION NAME(S) AND ADDRESS(ES)	8. PERFORMING ORGANIZATION REPORT NUMBER
DEVCOM Army Research Laboratory ATTN: FCDD-RLA-WA Aberdeen Proving Ground, MD 21005	ARL-TR-10307

9. SPONSORING/MONITORING AGENCY NAME(S) AND ADDRESS(ES)	10. SPONSOR/MONITOR'S ACRONYM(S)	11. SPONSOR/MONITOR'S REPORT NUMBER(S)

12. DISTRIBUTION/AVAILABILITY STATEMENT
DISTRIBUTION STATEMENT A. Approved for public release: distribution unlimited.

13. SUPPLEMENTARY NOTES
ORCID: Jennifer L. Gottfried, 0000-0002-1282-1928

14. ABSTRACT
The influence of chirality on the high-temperature chemistry and energy release behavior of the molecular ferroelectric salt imidazolium perchlorate ($ImClO_4$, or IM) with and without an external magnetic field was investigated. (*R*)-(+)-α-methylbenzylamine (R-MBA) and (*S*)-(−)-α-methylbenzylamine (S-MBA) chiral molecules were added to the IM to produce RIM and SIM, respectively. The addition of R-MBA and S-MBA decreased the total energy release from RIM and SIM compared to the neat IM but resulted in small differences in the chemistry and energy release behavior under the influence of the magnetic field.

15. SUBJECT TERMS
energetic material, molecular ferroelectric, magnetic field coupling, chirality, enantiomers, stereochemistry, laser-induced air shock from energetic materials, LASEM, Weapons Sciences

16. SECURITY CLASSIFICATION OF:			17. LIMITATION OF ABSTRACT	18. NUMBER OF PAGES
a. REPORT	b. ABSTRACT	C. THIS PAGE		
UNCLASSIFIED	UNCLASSIFIED	UNCLASSIFIED	UU	40

19a. NAME OF RESPONSIBLE PERSON	19b. PHONE NUMBER *(Include area code)*
Jennifer L. Gottfried	(520) 691-6002

STANDARD FORM 298 (REV. 5/2020)
Prescribed by ANSI Std. Z39.18

Contents

List of Figures

List of Tables

Acknowledgments

This work was funded by ARL's 6.2 project "Explosives for Long Range Collaborative Engagements" under the Long Range Distributed and Collaborative Engagements Essential Research Program in support of the Army's top modernization priority Long Range Precision Fires. The synthesis and development of the chiral ferroelectric crystals was funded by the Army Research Office under award W911NF-25-2-0038 (University of Maryland, College Park; principal investigator: Shenqiang Ren).

1. Introduction

Stereoisomerism is a classification for molecules with the same chemical formula and connectivity but a different spatial arrangement of atoms. Recently, several groups demonstrated the tunability of the physical properties of energetic materials (e.g., melt temperatures and sensitivities) by alteration of the stereo- and regiochemistry, where regioisomers are constitutional isomers with the same chemical formula but differing functional group positions or substituents (Figure 1).[1–6] At the U.S. Army Combat Capabilities Development Command (DEVCOM) Army Research Laboratory (ARL), the fast energy release from a series of nitroazetidine-based stereo- and regioisomers were compared using the laser-induced air shock from energetic materials (LASEM) technique.[7,8] The differences in estimated detonation velocities were attributed primarily to their relative purities, although the influence of stereochemistry could not be ruled out.

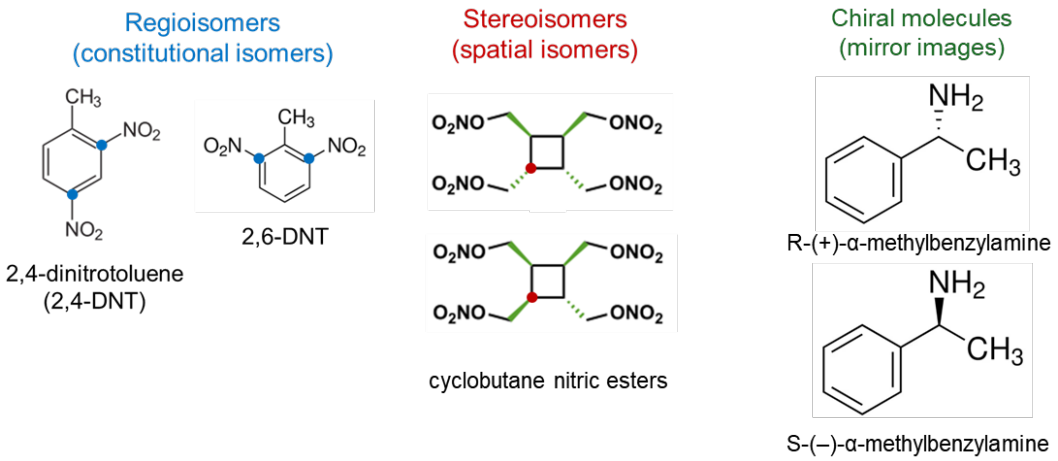

Figure 1. Examples of regioisomers, stereoisomers, and chiral molecules.

Chiral molecules are a subtype of stereoisomers called enantiomers, which are non-superimposable mirror-image stereoisomers (i.e., the property of being left- or right-"handed"). The chemical properties of a chiral molecule differ from those of its mirror image; for example, the relative orientations of chiral molecules can influence the trajectory of charge currents throughout the molecule and, potentially, their molecular reactivity. The properties of chiral ferroelectrics[9–13] or chiral magnets[14–16] and their response to optical stimuli have been investigated, but the energetic properties of chiral molecules are relatively unexplored.

We previously investigated the energy release behavior of the molecular ferroelectric salt imidazolium perchlorate ($ImClO_4$) with[17] and without[18,19] an embedded magnet. Low-temperature heating sufficient to depolarize the $ImClO_4$ (IM) results in desorption of imidazole rings and significant morphological changes

at the atomic scale, but did not influence the microsecond timescale energy release—i.e., the estimated detonation velocities measured via LASEM were not affected by the polarization state, in contrast to observed behavior from the molecular energetic ferroelectric [Hdabco]ClO_4 (dabco=1,4-diazabicyclo[2.2.2] octane).[20] Magnetic-field–enhanced LASEM (B-LASEM) was used to investigate the influence of a 0.78 T field on the energy release of IM with layers of magnets containing chromium (Cr) and either lithium (Li) or vanadium (V).[17] In addition to significantly enhancing the combustion of the magnet-in-IM composites, the magnetic field resulted in lower estimated detonation temperatures and lower estimated detonation velocities for the neat IM and the Cr–V magnet (which had weaker magnetic coupling).

Here, (*R*)-(+)-α-methylbenzylamine (R-MBA) and (*S*)-(−)-α-methylbenzylamine chiral molecules (S-MBA) (see Figure 1) were employed to produce chiral ferroelectric energetic materials based on IM, denoted either RIM or SIM (with neat IM for comparison). A similar process was recently used to produce chiral organic magnets.[16] Differential scanning calorimetry (DSC) and thermogravimetric analysis (TGA) were used to compare the energy release at relatively low heating rates (10 °C/min). The energy release behavior at high heating rates comparable to those during a detonation (~10^{13} K/s) was investigated using both conventional LASEM without an external magnetic field and B-LASEM with the sample placed on a permanent magnet with a 0.78 T field.

2. Experimental

2.1 Materials

Chiral composite materials were created using IM combined with either R-MBA or S-MBA to produce RIM and SIM, respectively. Approximately 10 mg of each sample (IM, RIM, and SIM) was spread on double-sided tape affixed to a glass microscope slide—replicate slides were made for LASEM measurements with and without the external magnetic field. For LASEM measurements without the magnetic field, the sample slide was placed on a vertical stage such that the laser focus was just below the sample surface. For B-LASEM measurements, the sample slide was placed on top of the magnet edge at the same height relative to the laser focus.

2.2 Thermal Analysis

DSC and TGA data was collected simultaneously using an SDT 650 (TA Instruments). Samples were placed in alumina pans and run in an argon (Ar)

atmosphere. The heating rate was 10 °C/min to a maximum temperature of 1450 °C.

2.3 LASEM Setup

The B-LASEM setup (Figure 2) has been described in detail elsewhere[17,21,22]; without the permanent magnets, the system is configured for LASEM-420 measurements.[23] The laser-induced shock velocities were measured to quantitatively compare the microsecond timescale energy release using high-speed schlieren imaging (420,000 fps; 2.38 µs between frames; 369-ns exposure; 300-W arc lamp light source). For this investigation, a total of 20 laser shots were obtained for each sample, both with and without the 0.78 T magnetic field. The shock wave positions were rounded down to the nearest pixel by the custom MATLAB code.[24] Because the high-speed schlieren videos were inadvertently saved using different settings than those used for previous LASEM studies (lowest bits instead of highest bits), the images had to be manipulated prior to processing to enhance the visualization of the shock wave for the automated MATLAB analysis code[25,26]; the color images were imported into ImageJ as separate red–green–blue (RGB) slices and the green slices were extracted for analysis following brightness/contrast enhancement. Therefore, the calculated shock parameters were normalized to the IM values since they are not directly comparable to previous results (which are sensitive to the camera settings and image conditions).

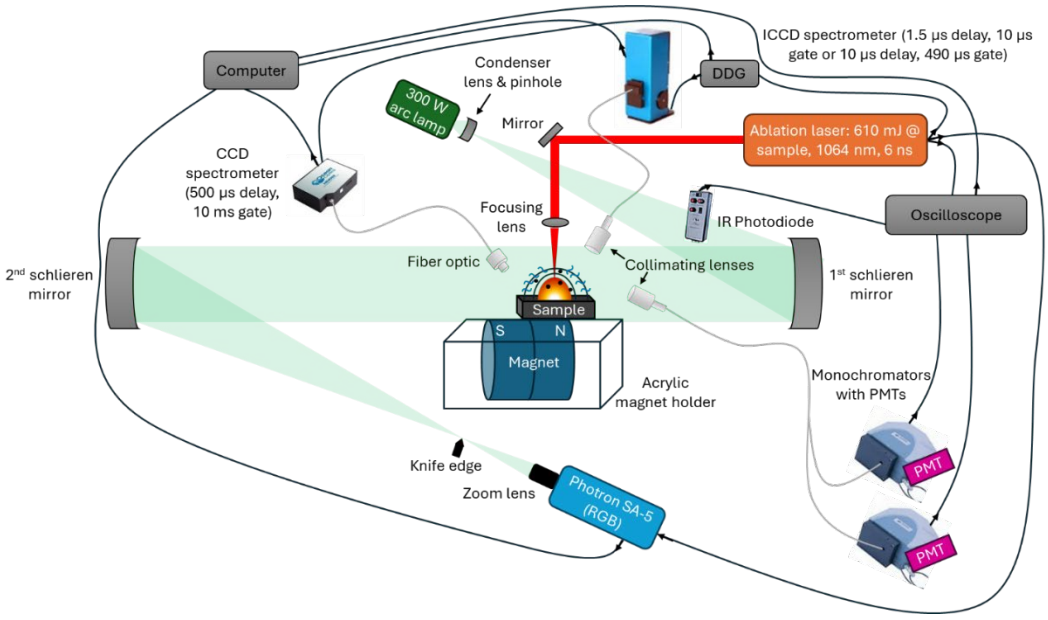

Figure 2. Experimental schematic for the B-LASEM system as configured for the current study; figure is not to scale.

In addition to measuring the laser-induced shock velocities, additional diagnostics were obtained to compare the emission from the laser-induced plasma (1.5–11.5 μs), post-plasma combustion (10–500 μs), and self-sustained combustion reactions (0.5–10.5 ms). The time-resolved emission for the hydrogen lines at 486 nm (H_β) and 656 nm (H_α) was recorded for the first five shots using monochromators with photomultiplier tube (PMT) detectors, as was the emission integrated over the infrared (IR) with a 10-MHz photoreceiver sensitive from 900 to 1700 nm. The self-sustained combustion emission spectra were also obtained for the first five (widely spaced) shots using a Czerny–Turner charge-coupled device (CCD) spectrometer (Ocean Optics HR4000, 230–900 nm). The post-plasma combustion emission spectra were obtained with a gated echelle spectrometer with intensified CCD (ICCD) (Catalina Scientific SE200, 200–1000 nm, $\lambda/\Delta\lambda = 2700$, gain = 900) for the first 10 shots. The laser-induced plasma spectra, which are less dependent on the amount of ejected material, were recorded for the last 10 shots using the ICCD spectrometer. All reported time-resolved data has been corrected for the instrument gains, which varied among the samples. The emission intensities used to calculate temperatures were corrected for the calibrated spectrometer response at the relevant wavelengths. All error bars in the figures represent the 95% confidence intervals based on the replicate data.

3. Results

3.1 Thermal Analysis

DSC traces up to 500 °C for all three compounds studied are shown in Figure 3. This temperature cutoff emphasizes the region of interest containing the first exotherm. The calculated enthalpies for the resulting exotherms were 1973.7 J/g for IM, 1835.2 J/g for RIM, and 1805.9 J/g for SIM; the exotherm enthalpies were lower because of the addition of the nonenergetic R-MBA or S-MBA. While RIM and SIM have slightly lower calculated enthalpies, these enthalpies are lower than that of IM only by about 100 J/g. In addition, there was no real enthalpy difference observed for RIM versus SIM. All three compounds have similar onset temperatures (~310 °C), although the peak exotherm temperature was lowest for RIM and highest for SIM.

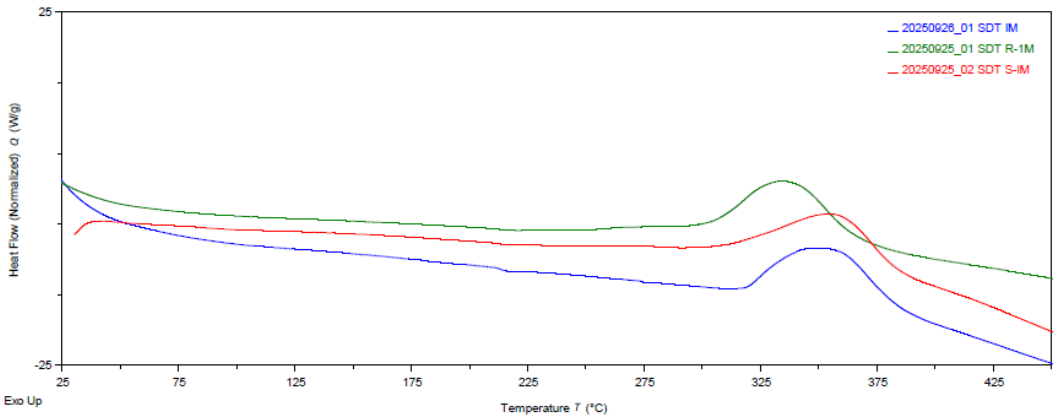

Figure 3. DSC results for IM, RIM, and SIM up to 500 °C.

The TGA traces for all three compounds are shown in Figure 4. Both RIM and SIM have more volatiles than neat IM, although all three compounds completely decomposed by 400 °C. Chirality does not appear to have a significant impact on the rate of decomposition or evaporation.

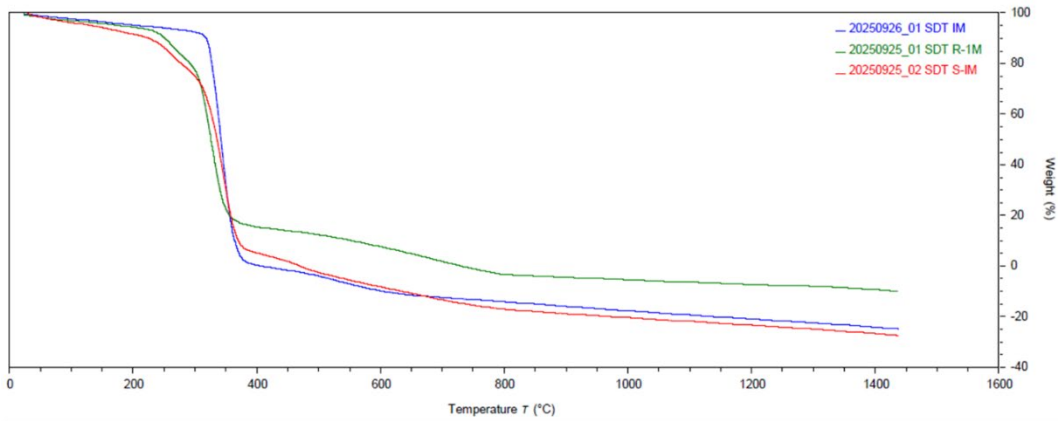

Figure 4. TGA results for IM (blue), RIM (green), and SIM (red) up to 1450 °C.

3.2 Laser-induced Shock Wave Measurements

Snapshots from the high-speed schlieren images are shown in Figure 5 following the postprocessing steps (including 90° clockwise rotation). The laser beam propagated from right to left and the subsequent expansion of the laser-induced plasma, combustion emission, and laser-induced shock wave propagated into the air above the sample from left to right. At the top of each image, the laser-induced plasma emission is visible for the first frame. This emission is significantly brighter for each sample without the magnetic field, which may indicate more rapid cooling of the laser-induced plasma in the presence of the magnetic field. The laser-induced shock wave could not be visualized in this first frame under the current image settings. The schlieren imaging also shows the height of the hot, gaseous plume

from the laser-initiated chemical reactions. The heights of the plumes in the last frame shown in Figure 5 (at 66.7 μs) are compared in Table 1. The height of the IM gaseous plume increases under a magnetic field, while it decreases for RIM and especially SIM.

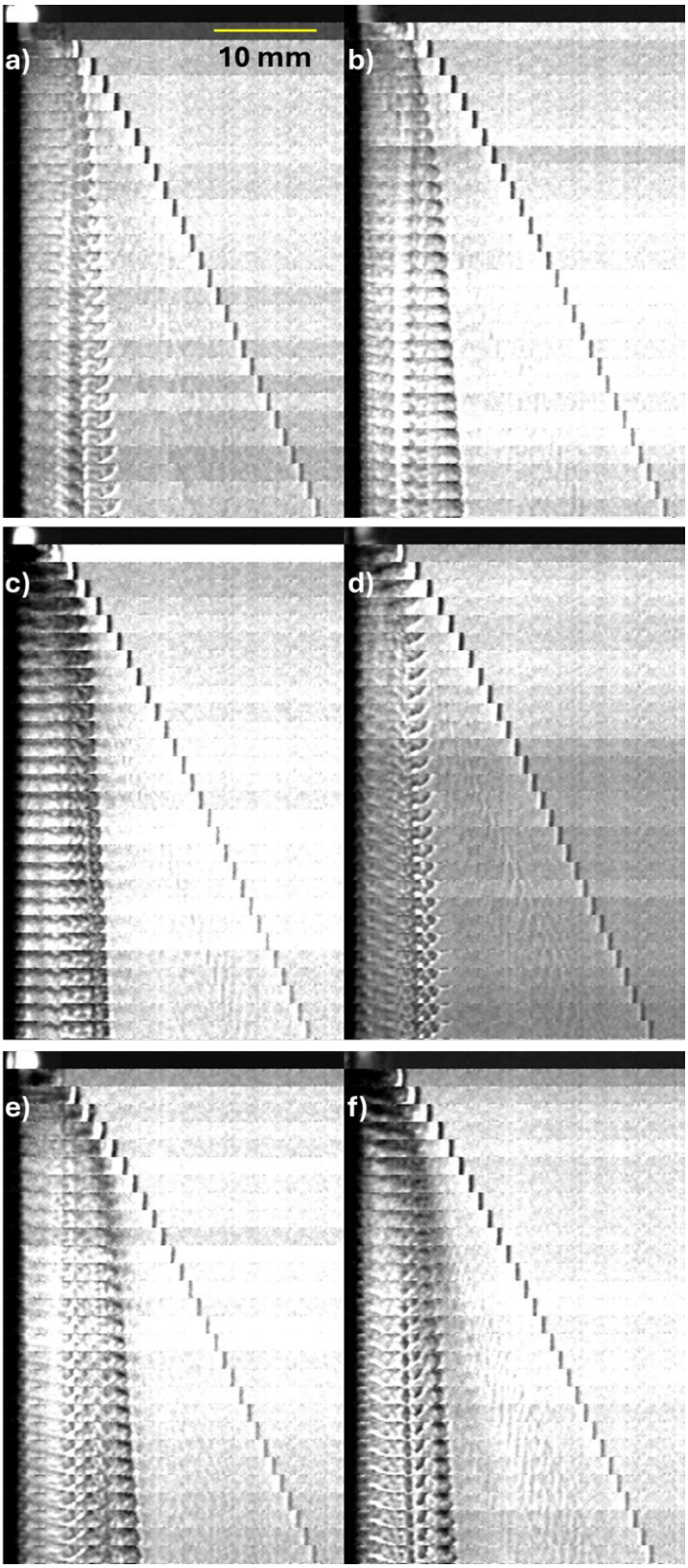

Figure 5. Snapshots from the high-speed schlieren videos for a) IM, b) IM (0.78 T), c) RIM, d) RIM (0.78 T), e) SIM, and f) SIM (0.78 T). Scale bar applies to all images.

Table 1. Gaseous plume height for each sample at 66.7 μs after the laser pulse.

Sample	Plume height at 0 T (mm)	Plume height at 0.78 T (mm)	Difference (%)
IM	9.6	10.5	8.6
RIM	9.6	8.6	–11.1
SIM	12.5	10.0	–20.0

Custom MATLAB code was used to determine the laser-induced shock wave position in each video frame (with the first five positions determined manually) and to fit the shock velocity versus time to various empirical or model-based fits.[25] The characteristic laser-induced shock velocity is defined as the y-intercept of a fifth-order polynomial fit to the shock velocity data—it quantifies the early microsecond timescale energy release in the laser-induced plasma and has been directly correlated to the measured detonation velocities extrapolated to the theoretical maximum density for explosives.[26–28] The Dewey shock velocity is defined as the value of the Dewey fit to the shock velocities at 13 μs—it quantifies the total energy release in the laser-induced plasma.[29] Figure 6 thus compares the early microsecond timescale energy release in the laser-induced plasma (y-axis) to the total energy release in the plasma (x-axis). The IM without the magnetic field has the highest characteristic and Dewey shock velocities. The decrease in characteristic laser-induced shock velocity for IM under the 0.78 T magnetic field was previously observed, although the change in Dewey shock velocity was not significant for that particular batch of material.[17] While the Dewey shock velocities for both IM and SIM decrease in this study, it increases for SIM. The RIM and SIM have lower shock velocities than IM due to the presence of the nonenergetic chiral methylbenzylamine (MBA).

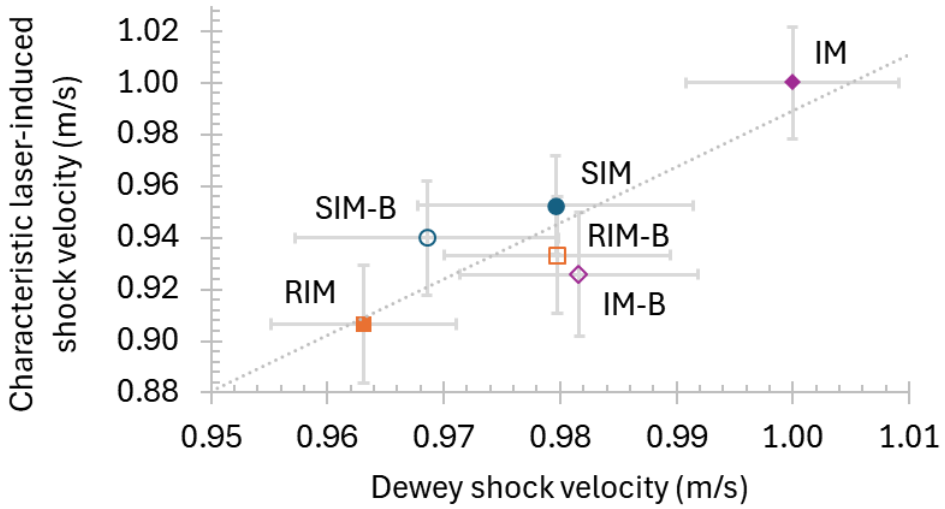

Figure 6. Correlation between the early microsecond timescale release (characteristic laser-induced shock velocities extrapolated to time zero) of each sample with (open symbols) and without (solid symbols) the magnetic field and the energy release after cessation of the laser-induced plasma (Dewey shock at 13 μs). The dotted line is a linear fit of the entire data set to guide the eye and the "–B" notation indicates the presence of the 0.78 T magnetic field.

Figure 7 compares the Sedov–Taylor energies (i.e., the energy added to the laser-induced plasma by the chemical reactions of each sample) based on the averaged shock data. No significant difference in energies was observed for the IM with or without the magnetic field, while the reaction energies of both RIM and SIM decreased—which roughly correlates with the observed plume height behavior suggesting fewer gaseous products were produced within the magnetic field of the chiral samples (Table 1). However, the observed increase in Dewey shock velocity for RIM-B (Figure 4) suggests some other difference in reaction mechanism leading to energy release for the RIM sample.

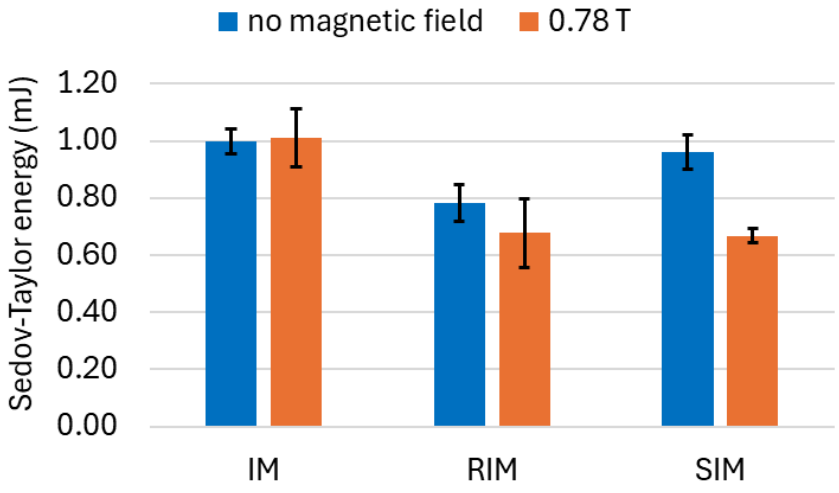

Figure 7. Sedov–Taylor energies from the reactions in the laser-induced plasma for each sample.

To confirm whether the observed differences in calculated shock parameters are statistically significant, analysis of variance (ANOVA) was performed using custom MATLAB code, followed by multiple comparison of means testing (Figure 8).[30] A small p value indicates that the observed differences are statistically significant (e.g., $p < 0.05$ indicates the means are statistically different at the 95% confidence level). These tests assume the data are normally distributed, which has been demonstrated previously for LASEM data.[23] For example, the characteristic laser-induced shock velocity for IM is significantly higher than all other samples, including IM-B, at greater than the 95% confidence level—but the values for RIM and RIM-B or SIM and SIM-B are not. On the later microsecond timescale, both IM and IM-B or RIM and RIM-B show significant differences in the Dewey shock velocity (lower or higher, respectively), while SIM and SIM-B do not. The Sedov–Taylor energies for RIM and RIM-B or SIM and SIM-B are significantly different, while those for IM and IM-B are not.

a)	IM	IM-B	RIM	RIM-B	SIM	SIM-B
IM		3.0E-06	1.4E-08	2.3E-05	2.4E-03	1.2E-04
IM-B	3.0E-06		2.0E-01	6.2E-01	7.9E-02	3.5E-01
RIM	1.4E-08	2.0E-01		7.9E-02	3.2E-03	2.9E-02
RIM-B	2.3E-05	6.2E-01	7.9E-02		2.0E-01	6.6E-01
SIM	2.4E-03	7.9E-02	3.2E-03	2.0E-01		4.0E-01
SIM-B	1.2E-04	3.5E-01	2.9E-02	6.6E-01	4.0E-01	

b)	IM	IM-B	RIM	RIM-B	SIM	SIM-B
IM		1.9E-02	9.6E-10	4.1E-02	3.0E-02	1.6E-04
IM-B	1.9E-02		2.6E-05	7.5E-01	8.8E-01	1.3E-01
RIM	9.6E-10	2.6E-05		7.4E-06	1.8E-05	5.0E-03
RIM-B	4.1E-02	7.5E-01	7.4E-06		8.7E-01	6.4E-02
SIM	3.0E-02	8.8E-01	1.8E-05	8.7E-01		9.6E-02
SIM-B	1.6E-04	1.3E-01	5.0E-03	6.4E-02	9.6E-02	

c)	IM	IM-B	RIM	RIM-B	SIM	SIM-B
IM		1.2E-01	3.8E-09	3.3E-02	2.6E-01	9.0E-06
IM-B	1.2E-01		3.0E-06	5.4E-01	6.8E-01	2.2E-03
RIM	3.8E-09	3.0E-06		3.5E-05	6.9E-07	7.0E-02
RIM-B	3.3E-02	5.4E-01	3.5E-05		3.1E-01	1.3E-02
SIM	2.6E-01	6.8E-01	6.9E-07	3.1E-01		6.6E-04
SIM-B	9.0E-06	2.2E-03	7.0E-02	1.3E-02	6.6E-04	

Figure 8. Multiple comparison of mean test results for the a) characteristic laser-induced shock velocities, b) Dewey shock velocities, and c) Sedov–Taylor energies; p values <0.05 (orange or red) indicate the means are statistically different with greater than 95% confidence.

3.3 Laser-induced Plasma Spectroscopy

The emission from the laser-induced plasma was obtained to improve our understanding of the high-temperature plasma reactions and compare compositional differences. The emission spectrum of the current IM sample (Figure 9a) has the expected features including lines resulting from carbon (C),

hydrogen (H), nitrogen (N), oxygen (O), chlorine (Cl), and cyano radical (CN). Common alkali and alkaline earth metal impurities typically originating from residual solvents were observed including lithium (Li), sodium (Na), and calcium (Ca). Additional metal impurities observed include magnesium (Mg) and aluminum (Al); all emission features were observed in the previous lot of IM[17] except Mg. The overall emission spectra for RIM (Figure 9b) and SIM (Figure 9c) are weaker than that of IM and include additional emission features such as diatomic carbon (C_2) and potassium (K). The emission spectrum of SIM shows emission features due to iron (Fe) that disappear under the magnetic field; the source of the Fe contamination is unknown. The unknown peak in the SIM spectra near 727.7 nm corresponds to the location of an indium (In) emission line, but without other confirmatory In lines (or an indication of the potential contamination source) it is difficult to definitely assign the feature.

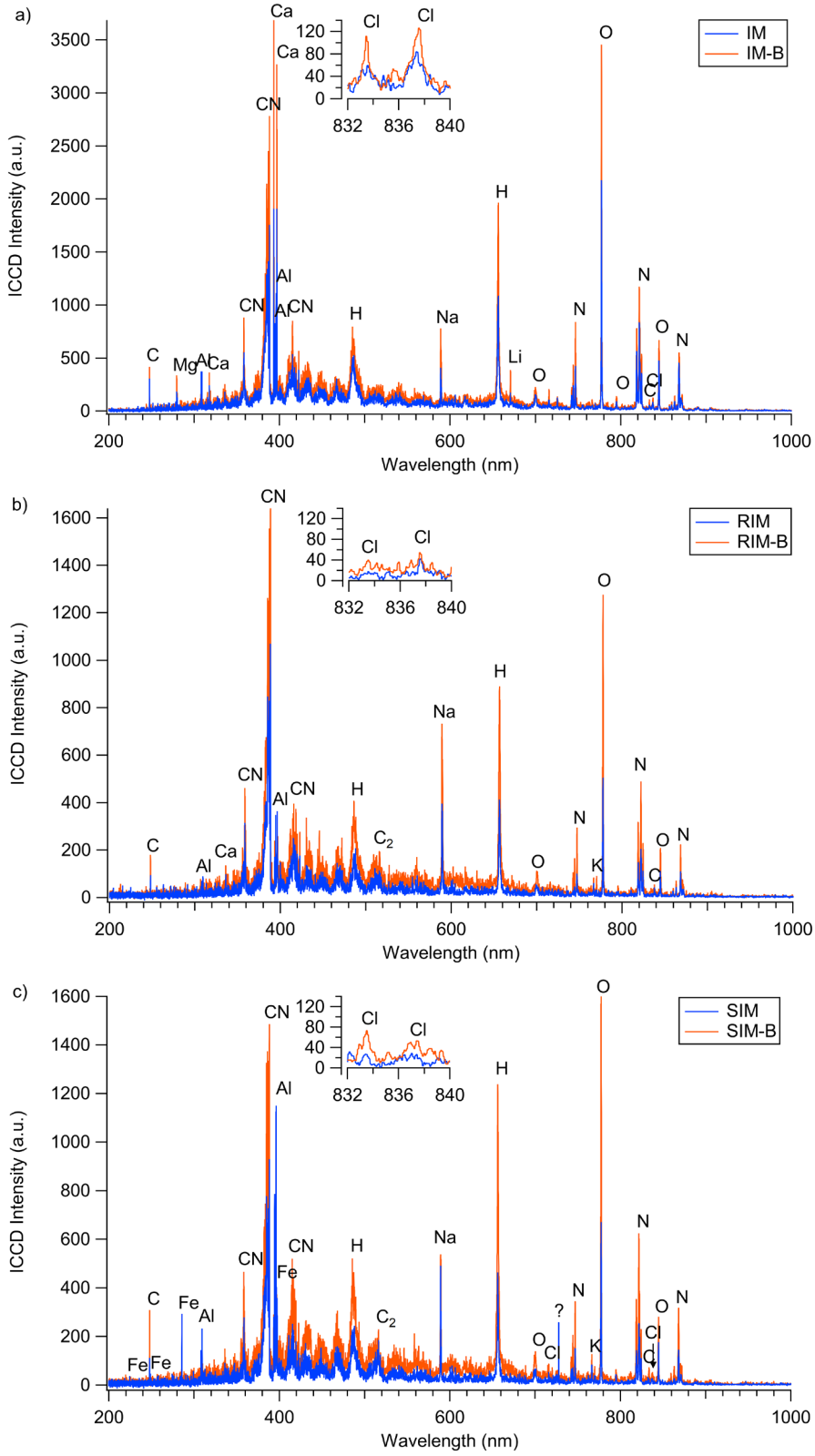

Figure 9. Laser-induced plasma spectra (1.5–11.5 µs) for the a) IM, b) RIM, and c) SIM with (orange) and without (blue) the 0.78 T magnetic field.

Figure 10 shows that the plasma emission is more intense in the presence of the magnetic field (based on the summed emission intensities of selected emission features), while Figure 5 suggests that the plasma is shorter-lived (i.e., less intense emission captured in the first high-speed video frame). The values from the previous batch of IM[17] are shown for comparison to the current lot.

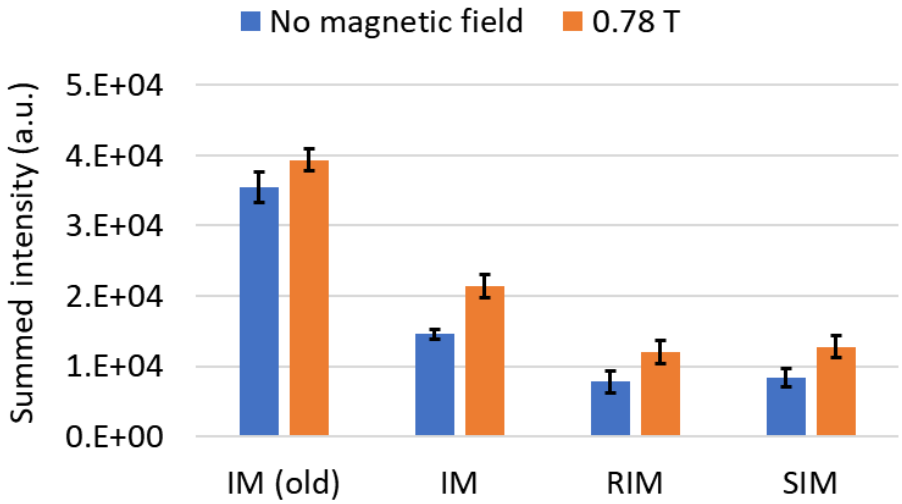

Figure 10. Summed emission intensities from the laser-induced plasma spectra of a previous batch of IM,[17] the current IM batch, and the RIM and SIM samples with (orange) and without (blue) the magnetic field.

Selected background-corrected, peak emission intensities were normalized to the summed emission intensities and are shown in Figure 11. Differences in the observed behavior for IM depend on the specific material lot and could be related to variances in the synthesis processes or post-synthesis storage (e.g., amount of adsorbed water). Generally, the peak emission intensities increase under the influence of the external magnetic field—although the C and O emission for the current lot of IM does not significantly change (in contrast to the previous lot). The increase in H for the previous lot of IM under the magnetic field is also significantly stronger than for the current IM lot. The normalized Cl emission for all samples is either not affected by magnetic field or decreases slightly.

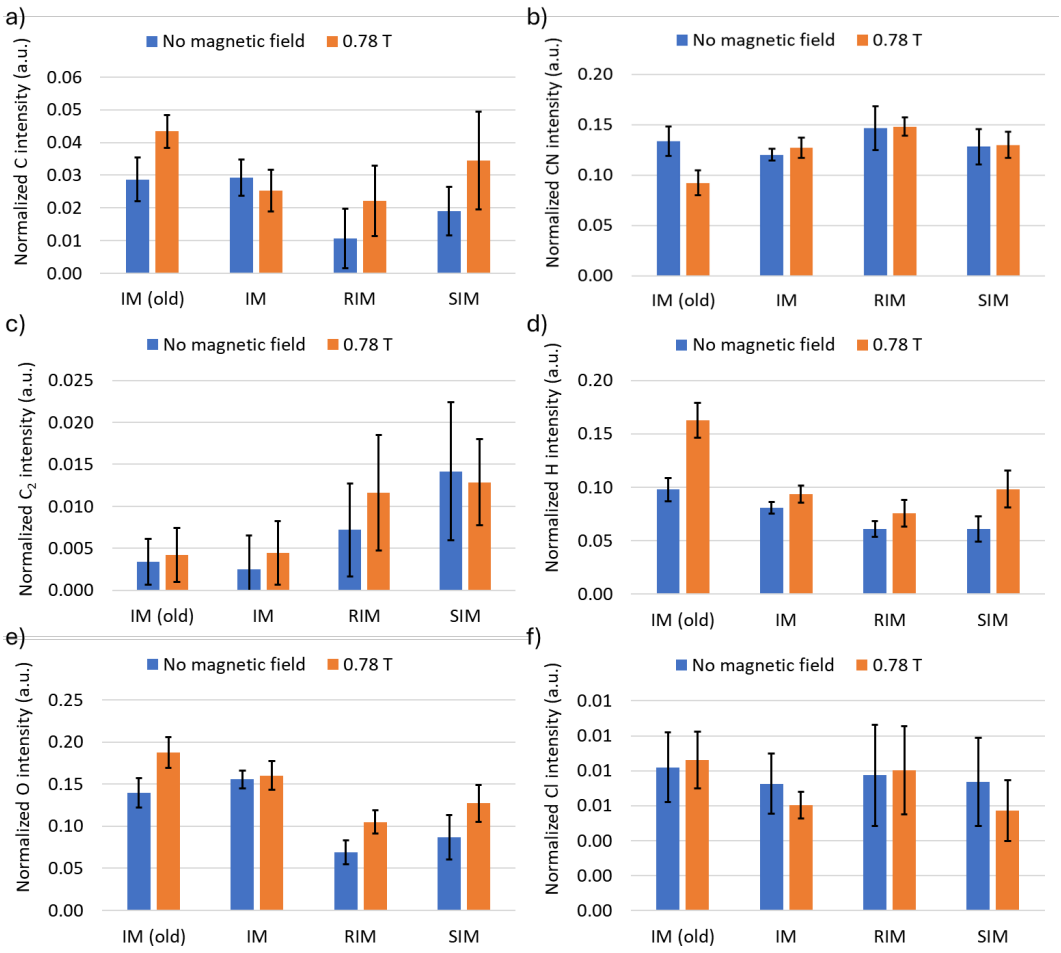

Figure 11. Normalized a) C (247.86 nm), b) CN (388.22 nm), c) C_2 (516.52 nm), d) H (656.29 nm), e) O (777.19/42 nm), and f) Cl (837.59 nm) emission from the laser-induced plasma spectra of the previous batch of IM[17] and the current IM, RIM, and SIM samples with (orange) and without (blue) the magnetic field.

Plasma excitation temperatures calculated based on the spatially and temporally averaged relative intensities of the H lines (434.05, 486.14, and 656.29 nm) are shown in Figure 12a. For conventional military explosives, we showed that these plasma excitation temperatures directly correlate to predicted detonation temperatures.[23] The plasma excitation temperature decreases under the influence of the magnetic field. Vibrational temperatures based on the relative intensities of the CN bands (388.22, 387.00, 386.03, 385.32, and 384.91 nm) were also calculated (Figure 12b). These temperatures decreased under the magnetic field for IM, significantly decreased for RIM, and increased slightly for SIM.

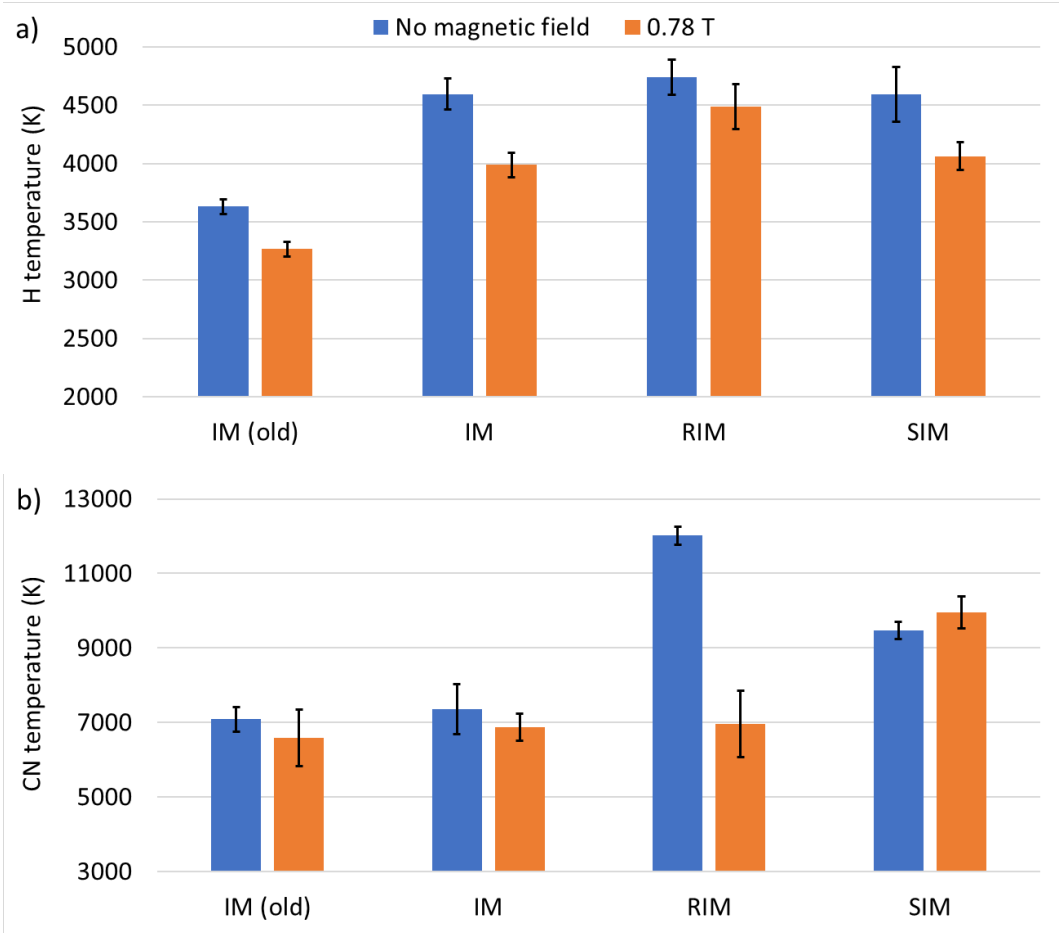

Figure 12. Calculated plasma a) excitation and b) vibrational temperatures from the laser-induced plasma spectra of the previous batch of IM[17] and the current IM, RIM, and SIM samples with (orange) and without (blue) the magnetic field.

Time-resolved plasma excitation temperatures were calculated using the relative intensities of the signals from the monochromator/PMTs set to record the H_α and H_β emission. One complication with these measurements is that the PMTs were saturated at times less than approximately 3 μs because of the intense continuum emission from the laser-induced plasma due to the Bremsstrahlung reactions of accelerating electrons. One million data points were recorded for each signal to preserve the high fidelity of the data on both the microsecond and millisecond timescales—therefore, 100-point binomial smoothing was used to reduce the noise in the calculated time-resolved temperature data. In addition, nonsensical temperatures less than zero or greater than 30,000 K were discarded.

The original PMT signals and calculated temperatures are shown for IM in Figure 13. No significant differences in the time-resolved plasma excitation temperature occur under the magnetic field, although the average temperature is slightly higher without the magnetic field. This trend agrees with the temperatures

averaged over the plasma lifetime (using 3 H line intensities), which are lower for IM under the magnetic field (Figure 12a). However, at times less than 3 μs the excitation temperature is higher with the magnetic field—which could explain the reduction in observed plasma emission (Figure 5) since higher peak temperatures lead to faster radiative cooling of the plasma.

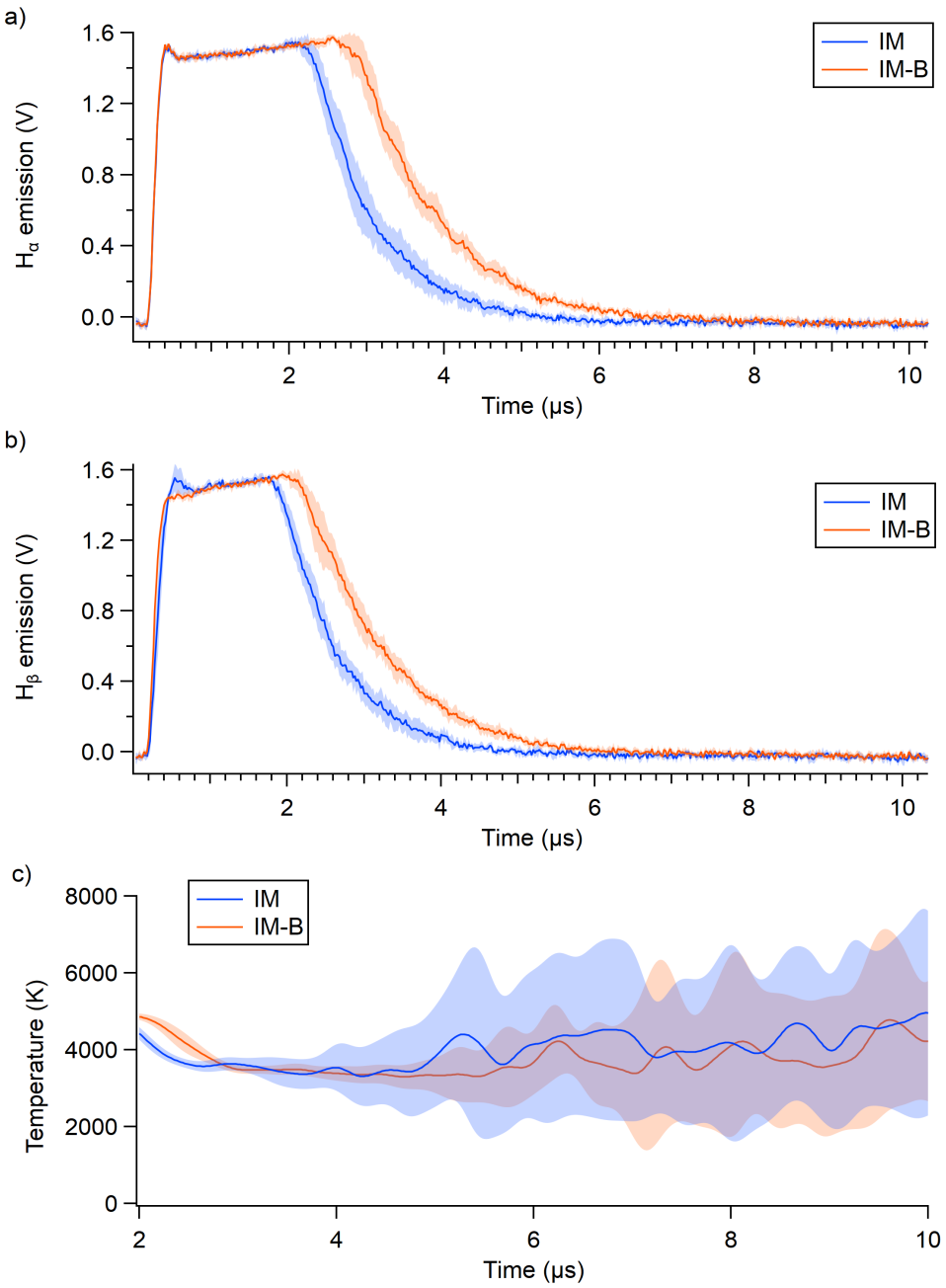

Figure 13. Time-resolved a) H_α, b) H_β, and c) plasma excitation temperatures for the IM samples with (orange) and without (blue) the magnetic field. Shaded regions indicate 95% confidence intervals.

The shot-to-shot variations in the time-resolved H emission signals for RIM decrease significantly in the presence of the magnetic field (Figure 14a,b). As with the IM, the time-resolved plasma excitation temperatures for RIM without the magnetic field are higher after about 2.7 µs; before that, the temperatures are higher with the magnetic field (Figure 14c).

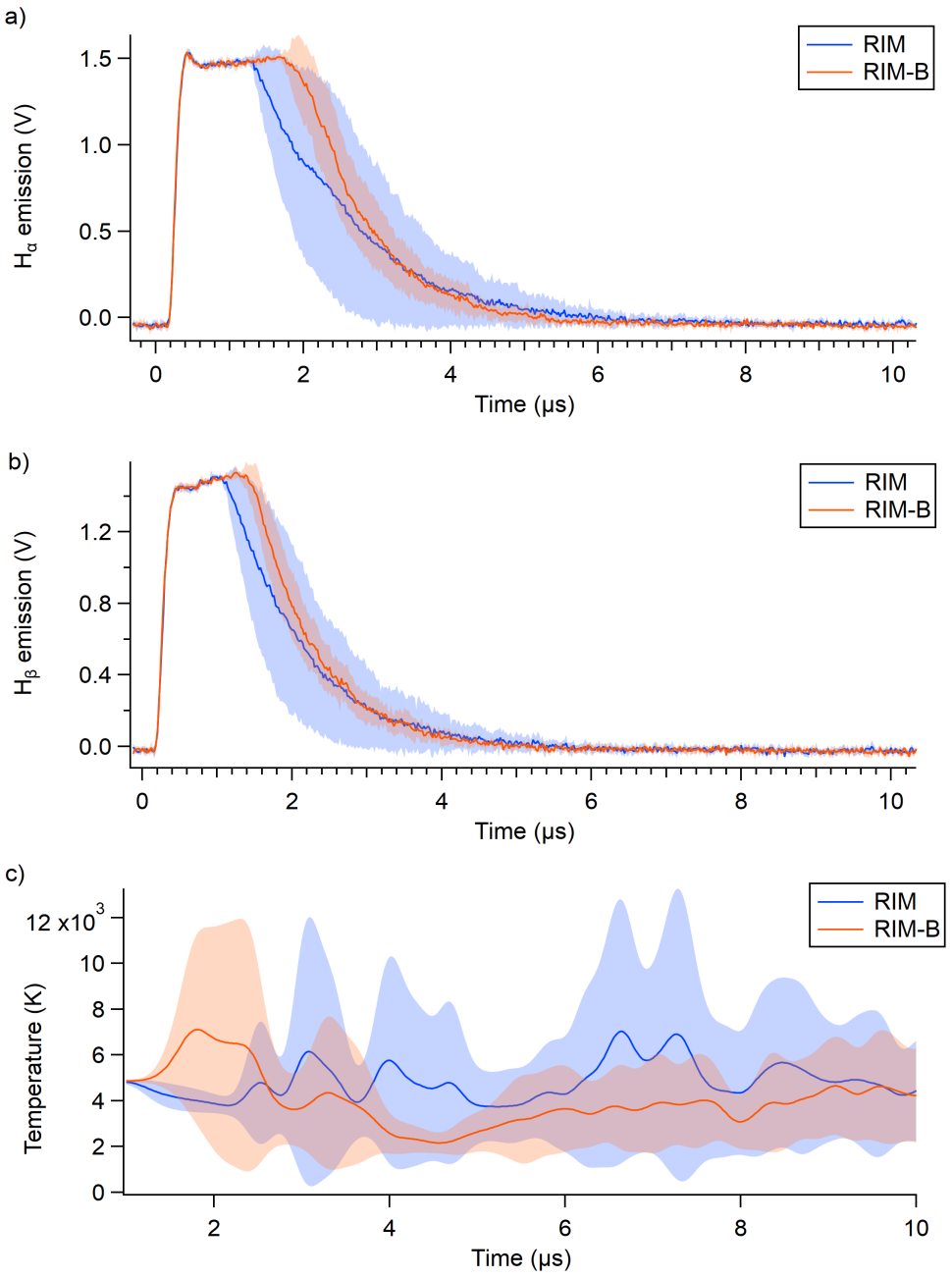

Figure 14. Time-resolved a) H_α, b) H_β, and c) plasma excitation temperatures for the RIM samples with (orange) and without (blue) the magnetic field. Shaded regions indicate 95% confidence intervals.

In contrast to the RIM, the shot-to-shot variations in H signal for the SIM increased in the presence of the magnetic field (Figure 15a,b). Although the time-resolved plasma excitation temperatures for SIM were similar with or without the magnetic field, they were slightly higher with the magnetic field at times less than about 5 µs (Figure 15c).

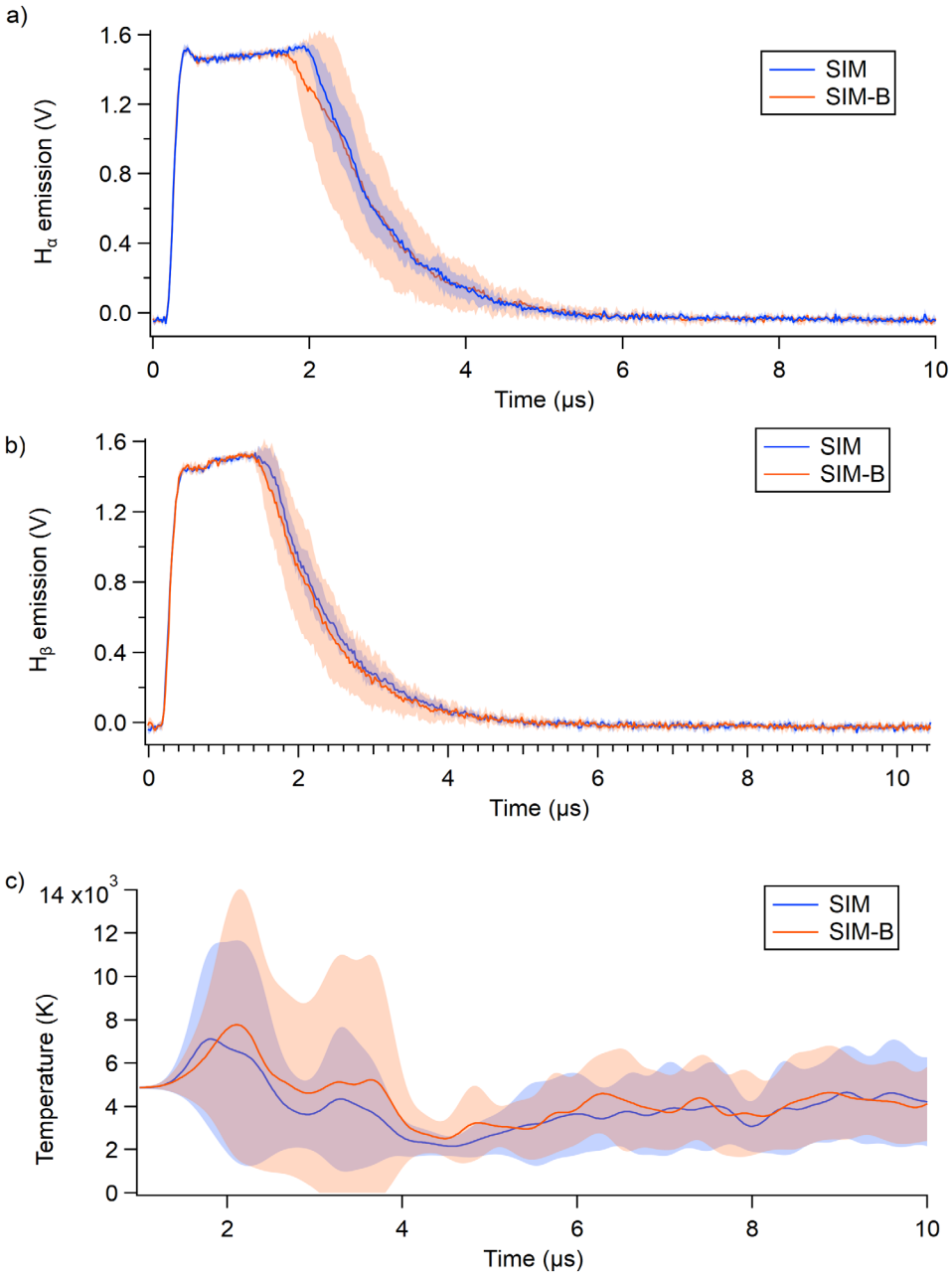

Figure 15. Time-resolved a) H_α, b) H_β, and c) plasma excitation temperatures for the SIM samples with (orange) and without (blue) the magnetic field. Shaded regions indicate 95% confidence intervals.

The plasma electron densities (Figure 16) were calculated based on the full width at half area of the averaged 656.29-nm H line using the method of Gigosos et al.[31] The presence of the magnetic field decreases the electron density for IM and SIM, but increases it for RIM.

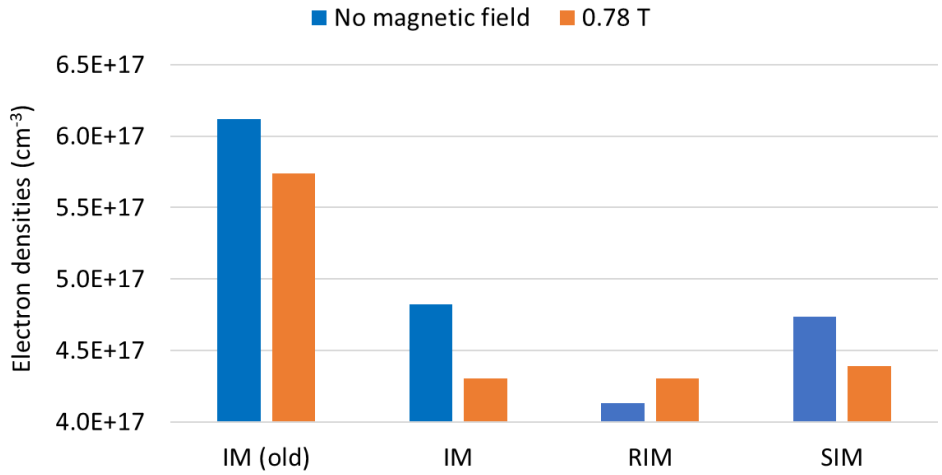

Figure 16. Calculated electron densities temperatures from the laser-induced plasma spectra of the previous batch of IM[17] and the current IM, RIM, and SIM samples with (orange) and without (blue) the magnetic field.

3.4 Post-Plasma Combustion Emission

Following cessation of the laser-induced plasma (as indicated by the disappearance of ionized species and emission from high-energy excited states), particles ejected from the sample surface continue to be ignited by the high-temperature region above the sample surface. This time regime (tens to hundreds of microseconds) thus consists of high-temperature combustion reactions. The post-plasma combustion spectra for each sample are shown in Figure 17. Under the influence of the magnetic field, the emission peaks from Ca, Na, Li, and K impurities increased in the IM spectra (Figure 17a), indicating additional combustion reactions resulting in continual excitation and de-excitation of those atoms occurred. An emission feature near 624 nm was present in all post-plasma combustion spectra and was tentatively assigned to silicon (Si). In addition, calcium chloride (CaCl) peaks appeared for the IM sample, indicating additional recombination reactions occurred in the presence of the magnetic field.

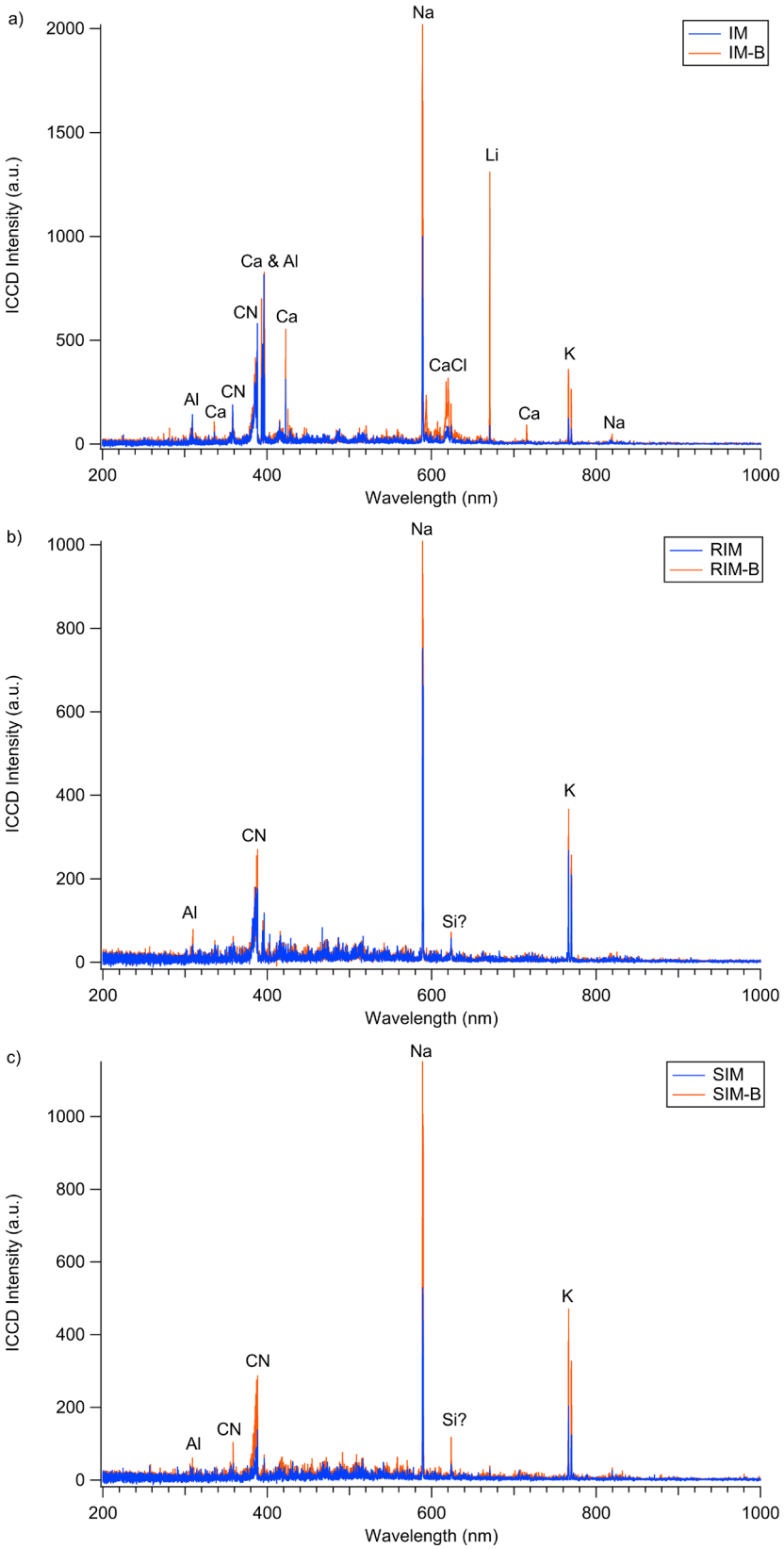

Figure 17. Post-plasma combustion spectra (10–500 µs) for the a) IM, b) RIM, and c) SIM with (orange) and without (blue) the magnetic field.

Both RIM (Figure 17b) and SIM (Figure 17c) have less IM content and significantly simpler post-plasma combustion spectra. Unlike with IM, the background-corrected, peak CN emission intensities increased for RIM and SIM in the presence of the magnetic field (Figure 18)—possibly due to the presence of R-MBA and S-MBA. The summed emission intensities across all wavelengths increased, to varying degrees, under the influence of the magnetic field for each sample (Figure 19).

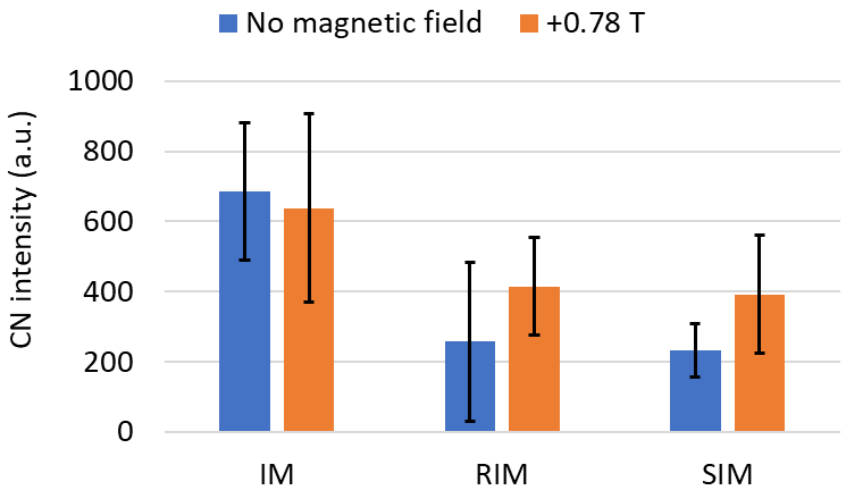

Figure 18. Normalized CN emission from the post-plasma combustion spectra of the IM, RIM, and SIM samples with (orange) and without (blue) the magnetic field.

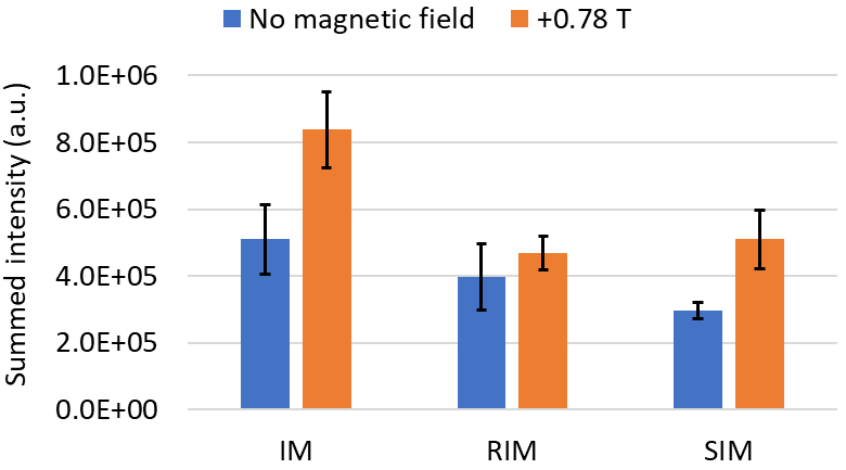

Figure 19. Summed post-plasma combustion emission intensities across all wavelengths for each sample with (orange) and without (blue) the magnetic field.

The time-resolved IR emission traces showed only slight differences in the post-plasma combustion regime (Figure 20). The IM showed a slight increase in IR emission from post-plasma combustion in the presence of the magnetic field (Figure 20a), while the effects of the magnetic field were more difficult to discern

for RIM (Figure 20b), largely because of the increase in shot-to-shot variation without the magnetic field, and SIM (Figure 20c), which had larger shot-to-shot variation with the magnetic field. Overall, the post-plasma combustion was quite weak for all samples, with or without the magnetic field.

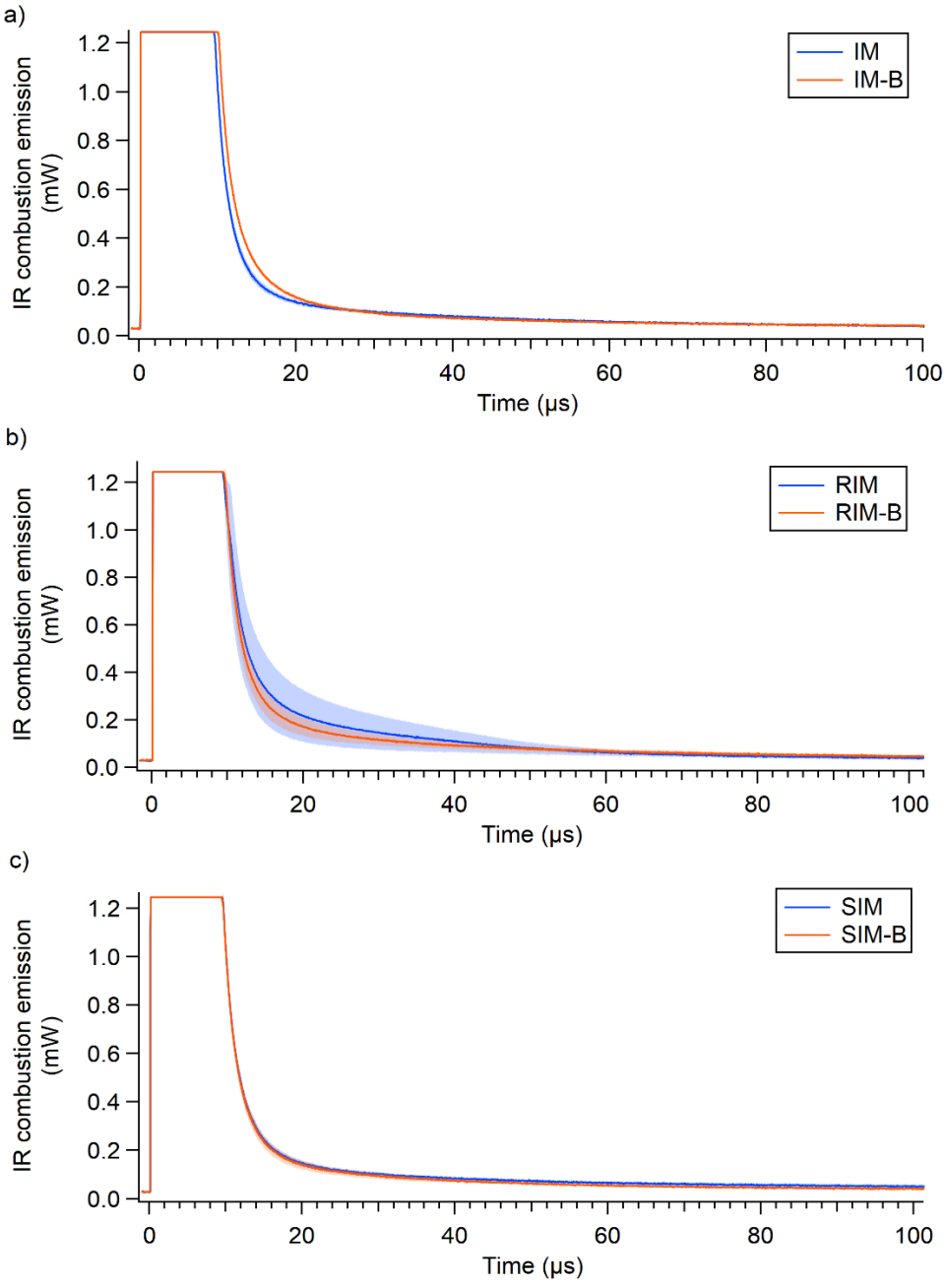

Figure 20. Time-resolved IR emission from the post-plasma combustion of the IM, RIM, and SIM samples with (orange) and without (blue) the magnetic field. Shaded regions indicate 95% confidence intervals.

3.5 Self-sustained Combustion Emission

The spectra from the self-sustained combustion reactions on the millisecond timescale are typically dominated by broadband blackbody radiation from the burning particles as well as having strong molecular emission bands. Although the time-resolved IR emission traces showed no evidence for additional combustion reactions beyond 100 μs (Figure 20), the emission spectra gated from 500 μs for 10 ms (Figure 21) did show weak emission lines from Ca and the hydroxyl radical (OH), a combustion intermediate. These features were significantly stronger in the presence of the magnetic field, indicating additional combustion reactions occurred.

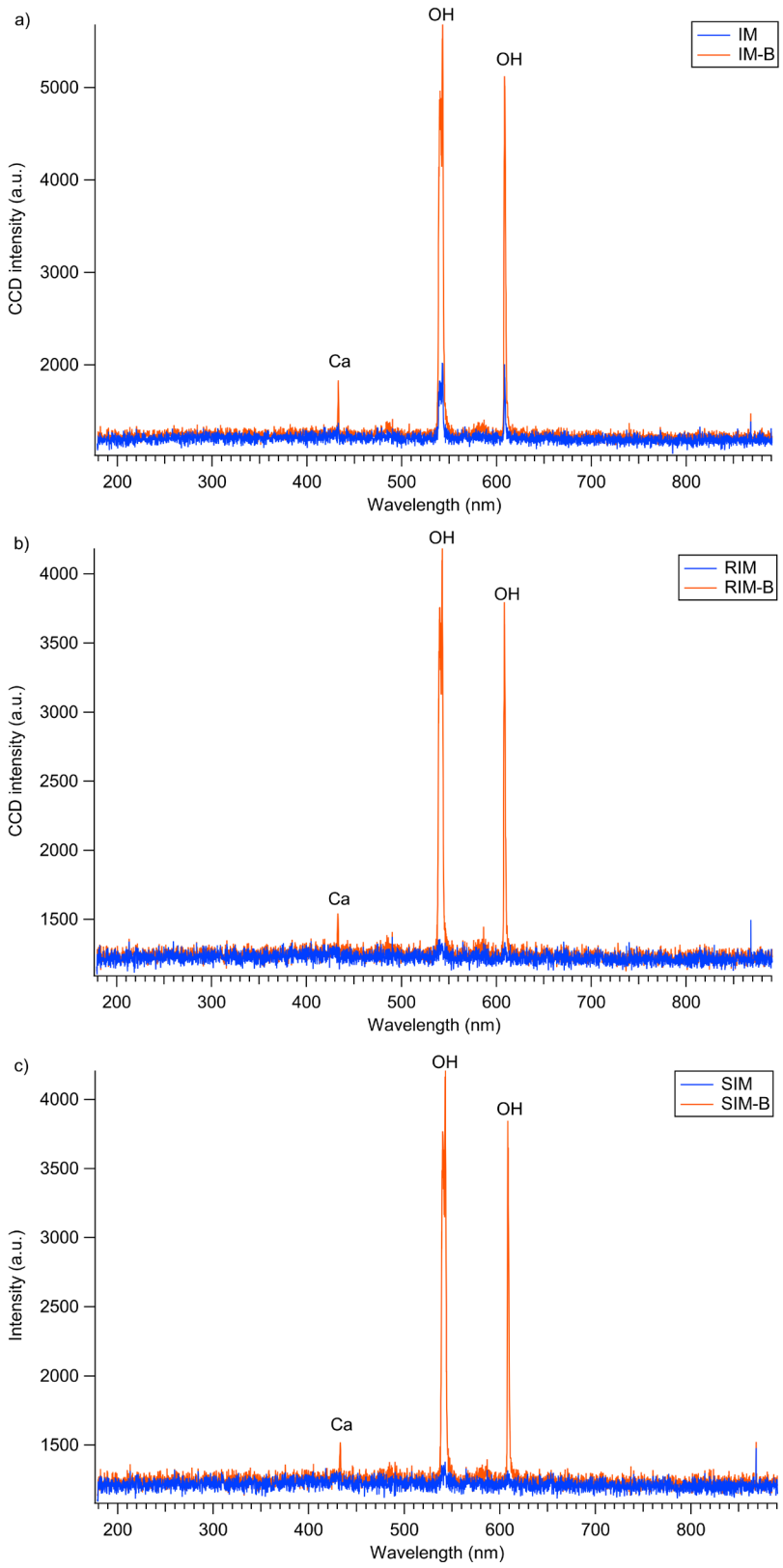

Figure 21. Self-sustained combustion spectra (500 µs–10.5 ms) for the a) IM, b) RIM, and c) SIM with (orange) and without (blue) the magnetic field.

4. Summary

Table 2 compares the experimental parameters measured in this study for each of the samples with or without the influence of the magnetic field. Differences between the IM and RIM or SIM were observed, presumably due to the incorporation of R-MBA or S-MBA to induce chirality and the subsequent chemistry changes. While some properties were universally affected by the magnetic field (e.g., plasma excitation temperatures and overall emission intensities), others were dependent on the chirality (e.g., Dewey shock velocities and plasma electron densities).

Table 2. Measured experimental parameters for each IM sample with and without the magnetic field.

Experimental parameter	IM (-B)	RIM (-B)	SIM (-B)
Exotherm enthalpy (J/g)	1973.7 (NA)	1835.2 (NA)	1805.9 (NA)
Peak exotherm temperature (°C)	~350 (NA)	~330 (NA)	~360 (NA)
Gaseous plume height at 66.7 μs (mm)	9.6 (10.5)	9.6 (8.6)	12.5 (10.0)
Relative characteristic shock velocity	1.00 ±0.02 (0.93 ±0.02)	0.91 ±0.02 (0.93 ±0.02)	0.95 ±0.02 (0.94 ±0.02)
Relative Dewey shock velocity	1.00 ±0.01 (0.98 ±0.01)	0.96 ±0.01 (0.98 ±0.01)	0.98 ±0.01 (0.97 ±0.01)
Sedov–Taylor energy (mJ)	1.00 ±0.04 (1.01 ±0.10)	0.78 ±0.06 (0.68 ±0.12)	0.96 ±0.06 (0.67 ±0.02)
Laser-induced plasma emission intensities (a.u.)	14540 ±712 (21366 ±1662)	7805 ±1542 (12009 ±1693)	8291±1281 (12761 ±1578)
Molecular species	CN, CaCl, OH (CN, CaCl, OH)	CN (CN, C_2, OH)	CN, C_2 (CN, C_2, OH)
Detected impurity species	Li, Na, Ca, Mg, Al, Si? (Li, Na, Ca, Mg, Al, Si?)	Na, Al, K, Si? (Na, Ca, Al, K, Si?)	Fe, Na, Al, K In?, Si? (Na, Al, K, Si?)
H excitation temperature (K)	4596 ±134 (3987 ±106)	4738 ±149 (4487 ±193)	4593 ±234 (4063 ±117)
CN vibrational temperature (K)	7355 ±678 (6876 ±364)	12014 ±240 (6963 ±888)	9468 ±230 (9952 ±422)
Electron density (10^{17} cm^{-3})	4.83 (4.30)	4.13 (4.30)	4.74 (4.39)

5. Conclusions

Some chemistry differences between the previous and current IM lots were observed, which may be due to the amount of adsorbed water or variations in the synthesis processes. Overall, the energy release was lower for RIM and SIM compared to IM because of the reduced IM content. Although the chirality did influence the chemistry and energy release rates for RIM and SIM under the magnetic field, this effect was quite small. The major observations from this study include the following:

- In general, the intensities of the spectral features from the laser-induced plasma increased for all IM samples under the magnetic field. Some species, such as Al and Fe, decreased under the magnetic field.
- Minor metal impurities (e.g., Al, Fe, Mg) were identified in the spectra of the IM samples.
- The plasma excitation temperatures decreased under the magnetic field (in contrast to previous studies that showed an increase in plasma temperature for some metals[22] or explosives[32] but similar to that observed for IM crystals with embedded magnets[17]). Time-resolved temperatures demonstrated that although the average temperature was lower under the magnetic field, early microsecond timescale temperatures were higher.
- The electron density in the laser-induced plasma decreased under the magnetic field for IM and SIM but increased for RIM.
- Both the enthalpy of the exotherm under slow heating conditions and the laser-induced shock velocities (microsecond timescale energy release) for RIM and SIM are lower than that of IM due to the presence of the nonenergetic chiral MBA material.
- No significant difference in early microsecond timescale energy release was observed for the chiral IM samples under the magnetic field compared to without the magnetic field.
- The differences in later microsecond timescale energy release with the magnetic field were only significant for the IM and RIM samples.
- Fewer gaseous products and less overall energy were produced from the laser-induced plasmas of the chiral IM samples—this effect was particularly pronounced for SIM.

6. References

1. Barton LM et al. Impact of stereo- and regiochemistry on energetic materials. J Am Chem Soc. 2019;141(32):12531–12535.
2. Wozniak DR, Salfer B, Zeller M, Byrd EFC, Piercey DG. Tailoring energetic sensitivity and classification through regioisomerism. Org Lett. 2020;22(22):9114–9117.
3. Zhai L et al. Exploring the highly dense energetic materials via regiochemical modulation: a comparative study of two fluorodinitromethyl-functionalized herringbone trifuroxans. Chem Eng J. 2020;391:123573.
4. Lv M, Zhou P, Ma Y, Li W, Liu J. The role of regioisomerism on thermal stability of furoxan based energetic materials. J Mol Struct. 2022;1262:132955.
5. Rykaczewski KA et al. Photochemical strategies enable the synthesis of tunable azetidine-based energetic materials. J Am Chem Soc. 2022;144(41):19089–19096.
6. Son J-Y et al. Exploring cuneanes as benzene isosteres and energetic materials: scope and mechanistic investigations into regioselective rear-rangements from cubanes. J Am Chem Soc. 2023;145(30).
7. Gottfried JL. Estimated detonation velocities for isomers of nitroazetidine polynitric esters and the "cartwheel of death." DEVCOM Army Research Laboratory (US); 2023 June. Report No.: ARL-TR-9706. (Report is CUI)
8. Gottfried JL, Schindler CS, Sabatini JJ. Estimated detonation performance of nitroazeditdine-based isomers. Presented at the 23rd Biennial Conference of the APS Topical Group on Shock Compression of Condensed Matter (APS GSCCM); 2023 June 18–23; Chicago, IL.
9. Gao W et al. Chiral molecular ferroelectrics with polarized optical effect and electroresistive switching. ACS Nano. 2017;11(11):11739–11745.
10. Liu H-Y, Zhang H-Y, Chen X-G, Xiong R-G. Molecular design principles for ferroelectrics: ferroelectrochemistry. J Am Chem Soc. 2020;142(36):15205–15218.
11. Chen HH et al. Spatial symmetry operation breaking sulfur-chiral photoswitchable ferroelectrics. J Am Chem Soc. 2025;147(12):10715–10723.

12. Wang Z, Wang Q, Quan L, Ren S. Reversible ferroelectric polarization modulation of chiral molecular ferroelectrics by circularly polarized light. Adv Sci. 2025;12(10):2414977.

13. Wang Z, Wang Q, Xiong YS, Quan L, Ren S. Chiral multiferroics for detection and imaging of circularly polarized light. 2025;25(35):13301–13306.

14. Wang Z et al. Organic chiral charge transfer magnets. ACS Nano 2019;13(4):4705–4711.

15. Gao M, Wang Z, Ren S, Hao X, Qin W. Organic chiral ferromagnets with strong spin-chiroptical interactions. Cell Rep Phys Sci. 2021;2(6):100442.

16. Wang ZX et al. Chiral molecular magnet superstructures with light control. Nano Lett. 2025;25(6):2502–2508.

17. Gottfried JL, Ren S. Influence of an external magnetic field on the reactions of magnet-in-ferroelectric energetic crystals. DEVCOM Army Research Laboratory (US); 2025 July. Report No.: ARL-TR-10127.

18. Gottfried JL, Wu C-C, Pesce-Rodriguez RA, Walck SD, Ren S. Imidazolium perchlorate: a novel energetic molecular ferroelectric. DEVCOM Army Research Laboratory (US); 2021. Report No.: ARL-TR-9289.

19. Hu Y et al. Chemically driven energetic molecular ferroelectrics. Nature Comm. 2021;12:5696.

20. Hu Y et al. Releasing chemical energy in spatially programmed ferroelectrics. Nature Comm. 2022;13(1):6959.

21. Gottfried JL, Dillier CAM, Wainwright ER. External magnetic field effects on the energy release from laser-ablated ferromagnetic, paramagnetic, and diamagnetic metals, part I: plates vs. powders under extremely weak magnetic fields. DEVCOM Army Research Laboratory (US); 2024 Aug. Report No.: ARL-TR-9958. (Report is CUI)

22. Gottfried JL, Dillier CAM. External magnetic field effects on the energy release from laser-ablated ferromagnetic, paramagnetic, and diamagnetic metals, part II: powders under moderately strong magnetic fields. DEVCOM Army Research Laboratory (US); 2025 June. Report No.: ARL-TR-10110. (Report is CUI)

23. Gottfried JL, Wainwright ER. Laser-induced air shock from energetic materials (LASEM): a novel microscale technique for characterizing energy release at high heating rates. J Energ Mater. 2023;43(1):1–61.

24. Gottfried JL. Automated shock wave measurement and fitting for the LASEM-420 system, part III: influence of pixel rounding errors. DEVCOM Army Research Laboratory (US); 2023 Dec. Report No.: ARL-TN-1184. (Report is CUI)

25. Gottfried JL, Dillier CAM, Wainwright ER. Automated shock wave measurement and fitting for the LASEM-420 system, part I: description of MATLAB codes. DEVCOM Army Research Laboratory (US); 2023 Aug. Report No.: ARL-TR-9738. (Report is CUI)

26. Gottfried JL, Dillier CAM, Wainwright ER. Automated shock wave measurement and fitting for the LASEM-420 system, part II: comparison of explosive data. DEVCOM Army Research Laboratory (US); 2023 Aug. Report No.: ARL-TR-9756. (Report is CUI)

27. Gottfried JL. Laboratory-scale method for estimating explosive performance from laser-induced shock waves. Propellants Explos Pyrotech. 2015;40(5):674–681.

28. Gottfried JL. Estimated detonation performance of Military explosives using higher time-resolution laser-induced air shock from energetic materials (LASEM-420): investigation of particle size effects for RDX and HMX. DEVCOM Army Research Laboratory (US); 2025 Mar. Report No.: ARL-TR-10073. (Report is CUI)

29. Wainwright ER, Gottfried JL. Monochromatic laser-induced shockwave measurements with improved data processing for reactive materials. DEVCOM Army Research Laboratory (US); 2021 May. Report No.: ARL-TR-9211.

30. Gottfried JL. Automated shock wave measurement and fitting for the LASEM-420 system, part IV: statistical significance of calculated parameters. DEVCOM Army Research Laboratory (US); 2024 Nov. Report No.: ARL-TN-1233. (Report is CUI)

31. Gigosos MA, González MÁ, Cardeñoso V. Computer simulated Balmer-alpha, -beta and -gamma Stark line profiles for non-equilibrium plasmas diagnostics. Spectrochim Acta Part B. 2003;58(8):1489–1504.

32. Gottfried JL. Magnetic field effects on the energy release of explosives, part I: HMX and RDX. DEVCOM Army Research Laboratory (US); 2026 Feb. Report No.: ARL-TR-10282. (Report is CUI)

List of Symbols, Abbreviations, and Acronyms

Al	Aluminum
ANOVA	Analysis of Variance
Ar	Argon
ARL	Army Research Laboratory
B-LASEM	Magnetic-field-enhanced LASEM
C	Carbon
C_2	Diatomic Carbon
Ca	Calcium
CCD	Charge-Coupled Device
Cl	Chlorine
CN	Cyano Radical
Cr	Chromium
DEVCOM	U.S. Army Combat Capabilities Development Command
DSC	Differential Scanning Calorimetry
Fe	Iron
H	Hydrogen
ICCD	Intensified Charge-Coupled Device
IM	$ImClO_4$
$ImClO_4$	Imidazolium Perchlorate
In	Indium
IR	Infrared
K	Potassium
LASEM	Laser-induced Air Shock from Energetic Materials
Li	Lithium
MBA	Methylbenzylamine
Mg	Magnesium

N	Nitrogen
Na	Sodium
NA	Not Applicable
O	Oxygen
PMT	Photomultiplier Tube
RGB	Red–Green–Blue
RIM	IM combined with R-MBA
R-MBA	(*R*)-(+)-α-methylbenzylamine
Si	Silicon
SIM	IM combined with S-MBA
S-MBA	(*S*)-(−)-α-methylbenzylamine
TGA	Thermogravimetric Analysis
V	Vanadium

1 (PDF)	DEFENSE TECHNICAL INFORMATION CTR DTIC OCA
1 (PDF)	DEVCOM ARL FCDD RLB CB TECH LIB